Simulations of Immuno-Contrast CT to Optimize Spectral Instrumentation and Nanoparticle Contrast Agent Materials

Matthew Tivnan[1], Grace Gang[2], and J. Webster Stayman[1]
[1]Department of Biomedical Engineering, Johns Hopkins University, Baltimore, MD
[2]Department of Radiology, Hospital of the University of Pennsylvania, Philadelphia, PA

Abstract Every year, new nanomedicines are developed for diagnostic and therapeutic applications. Antibody-tagged nanoparticles are particularly useful for targetting specific tissues. The current standard for preclinical evaluation of new antibody nanoparticles is positron emission tomography (PET) where the animals are divided into two groups, with one receiving the antibody nanoparticle and the other receiving a reference nanoparticle. However, there is significant mouse-to-mouse variation which means many mice must be scanned to make statistically significant claims about the effect of the antibody. With spectral CT and basis material decomposition one can potentially image the reference and antibody nanoparticles simultaneously in a single mouse. We propose a new type of functional imaging called *Immuno-Contrast CT* in which the reference nanoparticle distribution is subtracted from the antibody nanoparticle distribution to highlight the differential immunofunctional impact of the antibody. In this work we use physics simulations to jointly optimize contrast agent materials and spectral CT instrumentation for immuno-contrast CT. Our results show this optimization significantly reduces noise in the immuno-contrast images.

1 Introduction

Nanomedicine is a rapidly growing field that combines nanotechnology, immunology, and biomedical engineering to develop nanoparticles for diagnostic and therapeutic applications in medicine [1]. One particularly important area of research is the development of antibody-tagged nanoparticles that double as imaging contrast agents to target specific tissues or cell populations and highlight those areas in medical images [2] [3]. These antibody nanoparticles must be well-validated in a small animal model so that we understand the biological impact of the the nanoparticle before considering clinical use. Currently, one of the standard methods to determine the biodistribution of a nanoparticle with and without an antibody is to conduct a preclinical mouse imaging study with positron emission tomography (PET) [4] [5]. Typically, the mice are divided into two groups; one group would receive the antibody nanoparticle tagged with a radioisotope for PET imaging and the other group would receive a reference nanoparticle without the antibody. However, one problem with this type of PET imaging study is there can be significant mouse-to-mouse variation in the distribution of the nanoparticles. To test a hypothesis about the immunological function of a new antibody, one may need to use a large number of mice in order to have sufficient statistical power. Injecting so many mice with radioactive nanoparticles and scanning each mouse with a PET scanner can be a difficult and costly process and the final image results from PET often have low-spatial resolution and high-noise. In this work, we investigate the possibility of imaging nanoparticles with spectral x-ray computed tomography (CT). The key advantages over PET are 1) the ability to image the reference and antibody nanoparticles simultaneously in the same mouse using basis material decomposition 2) the lack of dependence on radioactive materials 3) higher spatial resolution with CT over PET.

Spectral CT uses x-ray projection measurements from multiple view angles and varied spectral sensitivity. This type of data can be used for three-dimensional tomographic image reconstruction as well as basis material decomposition. Spectral CT has already been used to image gold nanoparticles in mice [6] [7]. It has also been used to image iodine and gadolinium nanoparticles in mice simultaneously to characterize tumor vasculature [8] [9]. These studies show that imaging nanoparticles with spectral CT is a promising possibility. However, we know that material decomposition introduces noise relative to conventional CT images, so we expect that sensitivity to low concentrations of nanoparticles will be a challenging engineering problem.

We propose to investigate a new functional CT imaging method called *Immuno-Contrast CT* where a mouse is injected with both reference and antibody nanoparticles simultaneously. The two nanoparticles are labeled with two different CT contrast materials (e.g. iodine and gadolinium). Material decomposition permits reconstruction of separate image volumes for 1) water, 2) calcium, 3) reference nanoparticle concentrations, and 4) antibody nanoparticle concentrations. We define the *Immuno-Contrast Image* as the difference between the antibody nanoparticle image and the reference nanoparticle image. As a result, the immuno-contrast image will show the differential impact of the antibody on the biodistribution of the nanoparticle.

In this work, we use physical simulations of spectral CT systems to investigate different combinations of two contrast agent materials for immuno-contrast CT imaging and we simulate many spectral instrumentation designs and to answer three questions: 1) To what degree can we improve immuno-contrast CT image quality through intelligent spectral instrumentation design? 2) What are the optimal pair of contrast materials? 3) What are the optimal system designs pair of contrast materials? After this joint optimization, we evaluate our optimized design by generating a three-dimensional digital image volume with realistic mouse anatomy, simulating spectral measurements with x-ray sources and photon-counting detectors, and applying a model-based material decomposition algorithm to see the impact of our design optimization on immuno-contrast CT imaging performance.

2 Materials and Methods

2.1 Spectral CT Measurement Likelihood Model

Our mathematical model of spectral CT measurements is a random vector with a multivariate Gaussian distribution, $p(\mathbf{y}|\mathbf{x})$, parameterized by the mean, $\bar{\mathbf{y}}(\mathbf{x})$, and covariance, $\Sigma_{\mathbf{y}|\mathbf{x}}$. The mean is defined as

$$\bar{\mathbf{y}}(\mathbf{x}) = \mathbf{S}\exp(-\mathbf{Q}\mathbf{A}\mathbf{x}), \tag{1}$$

where $\mathbf{x}$ is a column vector of basis material densities for each voxel, $\mathbf{A}$ is the matrix of line integrals for each x-ray projection, $\mathbf{Q}$ is the basis material mass attenuation matrix, $\mathbf{S}$ is the

system spectral sensitivity matrix including all information about spectral sources and detectors, and $\mathbf{y}$ is a column vector of spectral CT measurements. Note, projection-domain material decomposition is a special case of this model where $\mathbf{A} = \mathbf{I}$. The negative log-likelihood is defined as

$$-\log \mathrm{p}(\mathbf{y}|\mathbf{x}) = \frac{1}{2}(\mathbf{y} - \bar{\mathbf{y}}(\mathbf{x}))^T {\Sigma_{\mathbf{y}|\mathbf{x}}}^{-1}(\mathbf{y} - \bar{\mathbf{y}}(\mathbf{x})) + c \quad (2)$$

where c is a constant with respect to $\mathbf{x}$ and $\mathbf{y}$.

2.2 Spectral CT Fisher Information Matrix and the Cramer-Rao Lower-Bound on Covariance

We aim to optimize spectral CT instrumentation by quantifying imaging performance as a function of the design matrices in (1). Specifically we are interested in jointly optimizing spectral instrumentation, described by $\mathbf{S}$, and contrast materials, described by $\mathbf{Q}$. This section defines a mathematical relationship between these design matrices and the Cramer-Rao Lower Bound (CRLB).

The Cramer-Rao inequality states that the covariance of an unbiased estimator is greater than or equal to inverse of the Fisher information matrix, $\mathbf{F}$. The definition of the Fisher information matrix is the Hessian, or second derivative, of the negative log-likelihood with respect to the vector $\mathbf{x}$. Taking the gradient of (2) yields

$$-\nabla_{\mathbf{x}} \log \mathrm{p}(\mathbf{y}|\mathbf{x}) = \mathbf{A}^T \mathbf{Q}^T \mathbf{D}_{\mathbf{x}}^T \mathbf{S}^T \Sigma_{\mathbf{y}|\mathbf{x}}^{-1}(\mathbf{y} - \bar{\mathbf{y}}(\mathbf{x})) \quad (3)$$

$$\mathbf{D}_{\mathbf{x}} = D\{\exp(-\mathbf{Q}\mathbf{A}\mathbf{x})\} \quad (4)$$

and so the Fisher information matrix is

$$\mathbf{F} = -\nabla_{\mathbf{x}}^2 \log \mathrm{p}(\mathbf{y}|\mathbf{x}) = \mathbf{A}^T \mathbf{Q}^T \mathbf{D}_{\mathbf{x}}^T \mathbf{S}^T \Sigma_{\mathbf{y}|\mathbf{x}}^{-1} \mathbf{S} \mathbf{D}_{\mathbf{x}} \mathbf{Q} \mathbf{A} \quad (5)$$

In this work, we use the CRLB, $\Sigma_{\mathbf{x}} \geq \mathbf{F}^{-1}$ to optimize spectral instrumentation design for immuno-contrast imaging. This predictive mathematical model describes the best-case-scenario for multi-material noise characteristics of unbiased material decomposition without the need to run a full material decomposition algorithm for each candidate design.

2.3 Simulations of Immuno-Contrast CT in Mice

We used the MOBY phantom [10] to generate three-dimensional digital image volumes of realistic mouse anatomy with 0.1 mm cubic voxels. For each voxel, there were four basis materials: water, calcium, the reference nanoparticle, and the antibody-labeled nanoparticle. To accomplish this, we ran the MOBY attenuation coefficient generator at 60 keV and 100 keV and analytically decomposed water/calcium basis image volumes. MOBY also has the ability to label activity level in specific tissues (usually for nuclear imaging simulations). We used the activity label images to define the concentration of reference and antibody nanoparticles in units of percent injected dose per gram (%ID/g). We used [5] as a rough guide for the biodistribution of reference nanoparticles and antibody nanoparticles which resulted in 15 %ID/g in the liver, 20 %ID/g in the spleen, 5 %ID/g in the kidney, and 2 %ID/g in the rest of the body for both the reference and antibody nanoparticles. We also inserted a 5 mm diameter spherical tumor into the liver which has 70 %ID/g for the antibody nanoparticle and 2 %ID/g for the reference nanoparticle. We assumed that the nanoparticle injections were 200 mL at 100 mg/mL to convert between %ID/g and mass density.

We used PYRO-NN [11], to model a cone beam forward projector, $\mathbf{A}$, with 1200 mm source-to-detector distance, 600 mm source-to-axis distance, and 0.2 mm square pixels. Our model for $\mathbf{Q}$ contains the mass attenuation spectra for water and calcium and two contrast materials. Our model for $\mathbf{S}$ is a polyenergetic x-ray source using the TASMICS model [12] with aluminium filtration as well as k-edge filtration computed using SPEKTR [13], and a photon counting detector. We do not include any model of non-ideal effects of photon counting detectors. We assume the detector has two energy bins per exposure and we have control over the energy threshold for three exposures. More details about the spectral instrumentation and contrast agent models are provided in the following section. For some select designs, we apply a projection-domain model-based material decomposition algorithm on a pixel-by-pixel basis using 1000 iterations of Newton's method to optimize the objective function in (2).

2.4 Optimization of Spectral CT Instrumentation and Nanoparticle Contrast Agent Materials

The goal of this work is to jointly optimize nanoparticle contrast agent materials and spectral instrumentation for immuno-contrast imaging. Therefore, our performance metric is the CRLB on the standard deviation in an immuno-contrast image formed by subtracting the reference nanoparticle image from the antibody nanoparticle image to highlight immuno-functional properties of the antibody.

For a given spectral design, $\mathbf{S}$, and set of basis materials, $\mathbf{Q}$, we consider one detector pixel in the projection domain and compute the cross-material Fisher information matrix using (5). We assume the background is 30 mm of water. Then we compute the CRLB by taking the matrix inverse and we compute the immuno-contrast variance using the formula $(\mathbf{w}^T \Sigma_{\mathbf{x}} \mathbf{w})/(\mathbf{w}^T \mathbf{w})$ where $\mathbf{w}$ is vector zero for water and calcium, positive one for the antibody nanoparticle, and negative one for the reference nanoparticle. This is equivalent to the noise variance in the immuno-contrast image. This process was repeated for the four material imaging scenario (water, calcium, X, Y) and three-material imaging scenario (water, X, Y). (We note that in the latter case, any calcium in the image volume will necessarily be modeled using the other basis materials. This model may have a potential noise advantage with fewer material bases but will generally bias material estimates.)

We evaluated the above performance metrics for 421,875 spectral designs and 10 combinations of two contrast materials for a total of over 4.2 million spectral CT imaging scenarios. The design parameters for the spectral source are: source voltage (60, 70, 80, 90, or 100 kVp), aluminium filter thickness (0.0, 0.5, 1.0, 2.0, or 4.0 mm), and k-edge filter (None, 250 μm Praseodymium, 250 μm Erbium, 125 μm Tantalum, or 125 μm Lead). The design parameters for the photon counting detector are: energy threshold for each of

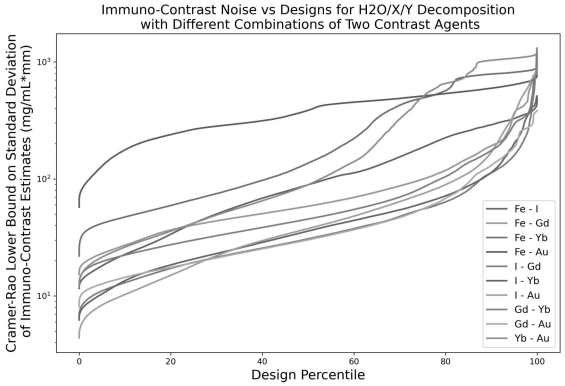

Figure 1: The CRLB for 4-material decomposition for all spectral designs and all contrast materials. Then the designs were sorted by immuno-contrast noise levels.

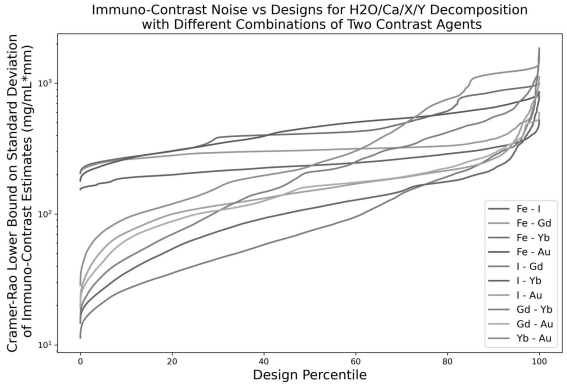

Figure 2: The CRLB for 3-material decomposition for all spectral designs and all contrast materials. Then the designs were sorted by immuno-contrast noise levels.

the three exposures (50, 60, 70, 80, or 90% of kVp) and exposure time for each of the three exposures (1, 2, or 3 relative exposure). Exposures were normalized such that incident x-ray fluence after source filtration is 10^6 photons per pixel per view. So, for example, if the three relative exposures are (1,1,1) then the number of incident photons is 3.33×10^5 for all three exposures, but if the three relative exposures are (1,1,3) then the first two exposures have 2.00×10^5 incident photons and the third exposure has 6.00×10^5 incident photons. Finally, we repeat the evaluation for all combinations of two contrast agent materials from among: Iron (Fe), Iodine (I), Gadolinium (Gd), Ytterbium (Yb), and Gold (Gd).

3 Results

The CRLB of immuno-contrast standard deviation is summarized for all designs in Figures 1 and 2. The three-material imaging case is shown in Figure 1 and the four-material case is shown in 2. For each contrast agent combination, we sorted the designs by immuno-contrast noise. The x-axis shows the design percentile and the y-axis shows our performance metric, the CRLB on immuno-contrast standard deviation. The 0th design percentile indicates the spectral designs with the best performance. We have summarized the performance of optimized spectral designs in Figure 3 and the optimized design parameters have been listed in table 1. Finally, the results of the model-based material decomposition are shown in Figures 4 5 and 6. Figure 4 shows the ground truth material density line integrals for this simulation. Figure 5 shows the material decomposition results for the 50th percentile system design and Figure 6 shows the 0th percentile top performing system design for H2O/Ca/I/Gd imaging.

4 Discussion

In Figures 1 and 2 we see that there is a wide range of performance levels for different spectral designs and different combinations of materials. There is a relatively steep falloff in performance relative to the best designs (near 0th percentile) which indicates that fine tuning the spectral sensitivity of the system can significantly reduce noise in the immuno-contrast images. In Figure 2 we see that all of the cases using iron as a contrast agent material have extremely high noise even for the optimized design. We believe this is due to the fact

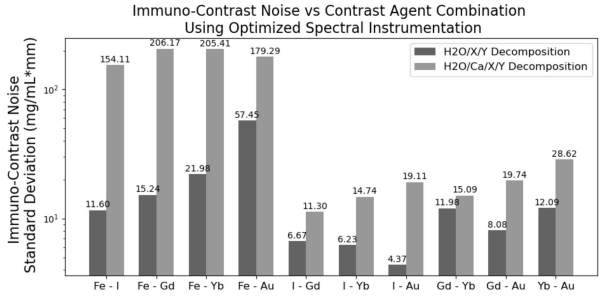

Figure 3: The Cramer-Rao lower bound on immuno-contrast noise standard deviation for all combinations of contrast agents using optimal spectral instrumentation.

that the k-edge of iron is much lower than the x-ray spectra of these designs. Therefore, water, calcium, and iron, are approximately linearly dependent on only two basis (e.g. photoelectric effect and Compton scattering). The contrast agents which achieved the lowest immuno-contrast noise for four-material decomposition were iodine and gadolinium. These are the same contrast agents used in [8, 9] so there is already evidence it is possible to image these two materials simultaneously in mice. The material decomposition results in Figures 4 5 and 6 show visible reduction of immuno-contrast noise for the optimized design relative to the 50th percentile. These results show that a 5 mm diameter lesion with realistic nanoparticle concentrations in visible with realistic x-ray fluence levels.

5 Conclusion

This simulation study is an early stage investigation to determine the feasibility of immuno-contrast CT imaging. There are several areas where we have made assumptions and idealized approximations about both the mouse biodistribution model and spectral CT imaging simulation and material decomposition. For example, we have assumed that the reference and antibody nanoparticle biodistributions are the same with the exception of the tumor. This may not be true in practice especially when using two different contrast materials. For the material decomposition algorithm, we used a perfectly matched reconstruction model to the data generation model. In practice it is very difficult to calibrate the sensitivity of spectral CT imaging systems.

Contrast Agents	Source kVp	Al Filter	K-Edge Filter	Exposure 1	Threshold 1	Exposure 2	Threshold 2	Exposure 3	Threshold 3
H2O-Ca-Fe-I	60.0 kVp	4.0 mm Al	250um Pr	2.00E+05	30.24 keV	6.00E+05	33.6 keV	2.00E+05	42.0 keV
H2O-Ca-Fe-Gd	60.0 kVp	0.5 mm Al	None	5.00E+05	25.92 keV	2.50E+05	28.8 keV	2.50E+05	48.0 keV
H2O-Ca-Fe-Yb	70.0 kVp	0.5 mm Al	None	5.00E+05	28.35 keV	1.67E+05	31.5 keV	3.33E+05	63.0 keV
H2O-Ca-Fe-Au	60.0 kVp	0.5 mm Al	None	5.00E+05	18.9 keV	3.33E+05	37.8 keV	1.67E+05	42.0 keV
H2O-Ca-I-Gd	70.0 kVp	4.0 mm Al	None	3.33E+05	30.24 keV	5.00E+05	50.4 keV	1.67E+05	63.0 keV
H2O-Ca-I-Yb	80.0 kVp	0.0 mm Al	125um Pb	4.29E+05	34.56 keV	1.43E+05	57.6 keV	4.29E+05	64.0 keV
H2O-Ca-I-Au	100.0 kVp	4.0 mm Al	250um Pr	2.00E+05	36.0 keV	2.00E+05	40 keV	6.00E+05	80.0 keV
H2O-Ca-Gd-Yb	90.0 kVp	4.0 mm Al	125um Ta	1.67E+05	45.36 keV	3.33E+05	50.4 keV	5.00E+05	63.0 keV
H2O-Ca-Gd-Au	100.0 kVp	4.0 mm Al	125um Pb	2.00E+05	44.8 keV	2.00E+05	56 keV	6.00E+05	80.0 keV
H2O-Ca-Yb-Au	100.0 kVp	4.0 mm Al	125um Pb	1.67E+05	38.4 keV	3.33E+05	64 keV	5.00E+05	80.0 keV
H2O-Fe-I	100.0 kVp	0.5 mm Al	None	5.00E+05	27.0 keV	3.33E+05	30 keV	1.67E+05	50.0 keV
H2O-Fe-Gd	100.0 kVp	1.0 mm Al	None	2.00E+05	40.5 keV	2.00E+05	45 keV	6.00E+05	50.0 keV
H2O-Fe-Yb	90.0 kVp	4.0 mm Al	250um Pr	2.00E+05	51.03 keV	2.00E+05	56.7 keV	6.00E+05	63.0 keV
H2O-Fe-Au	100.0 kVp	4.0 mm Al	250um Pr	2.00E+05	40.5 keV	6.00E+05	81 keV	2.00E+05	90.0 keV
H2O-I-Gd	80.0 kVp	0.0 mm Al	125um Ta	3.33E+05	45.36 keV	5.00E+05	50.4 keV	1.67E+05	56.0 keV
H2O-I-Yb	70.0 kVp	0.5 mm Al	None	4.29E+05	25.2 keV	4.29E+05	28 keV	1.43E+05	35.0 keV
H2O-I-Au	70.0 kVp	1.0 mm Al	None	3.33E+05	30.24 keV	5.00E+05	33.6 keV	1.67E+05	42.0 keV
H2O-Gd-Yb	70.0 kVp	4.0 mm Al	None	1.67E+05	39.69 keV	3.33E+05	44.1 keV	5.00E+05	49.0 keV
H2O-Gd-Au	70.0 kVp	4.0 mm Al	None	2.00E+05	45.36 keV	6.00E+05	50.4 keV	2.00E+05	56.0 keV
H2O-Yb-Au	80.0 kVp	2.0 mm Al	125um Pb	1.43E+05	51.84 keV	4.29E+05	57.6 keV	4.29E+05	64.0 keV

Table 1: Optimized spectral instrumentation design parameters for low immuno-contrast noise for each contrast material combination.

Despite the idealized conditions, we can draw some conclusions from the results of this preliminary investigation. First, immuno-contrast CT appears to be physically possible for realistic nanoparticle concentrations and x-ray exposure levels. Second, iodine and gadolinium are a good choice of contrast agents for immuno contrast imaging. Third, optimizing the spectral design for specific combinations materials can significantly reduce noise in the immuno-contrast images.

Immuno-contrast CT imaging has the potential to accelerate the development of nanomedicines because it can simultaneously image the reference and antibody nanoparticle biodistributions, improving the statistical power of preclinical imaging studies. In the future, we look forward to addressing some of these non-ideal effects and moving on to physical experiments with spectral CT imaging systems.

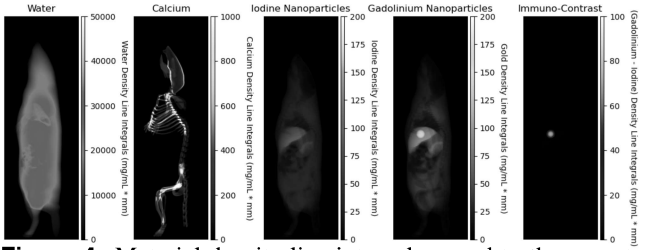

Figure 4: Material density line integral ground truth generated with the MOBY phantom. Immuno-contrast is Gd minus I.

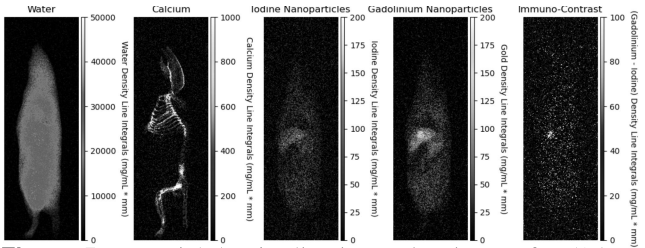

Figure 5: Material density line integral estimates for 50th percentile design for low immuno-contrast noise power.

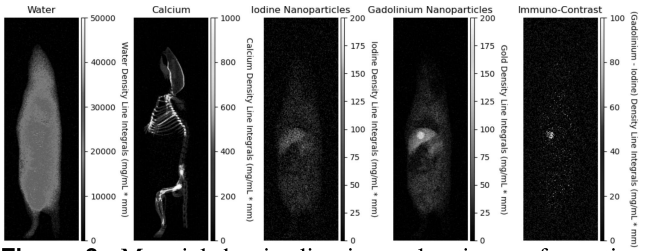

Figure 6: Material density line integral estimates for optimal design for low immuno-contrast noise power.

Acknowledgements

This work is supported in part by NIH Grant R01EB030494

References

[1] B. Y. Kim, J. T. Rutka, and W. C. Chan. "Nanomedicine". *New England Journal of Medicine* 363.25 (2010), pp. 2434–2443.

[2] F. Fay and C. J. Scott. "Antibody-targeted nanoparticles for cancer therapy". *Immunotherapy* 3.3 (2011), pp. 381–394.

[3] D. P. Cormode, P. C. Naha, and Z. A. Fayad. "Nanoparticle contrast agents for computed tomography: a focus on micelles". *Contrast media & molecular imaging* 9.1 (2014), pp. 37–52.

[4] G. A. Van Dongen, G. W. Visser, M. N. Lub-de Hooge, et al. "Immuno-PET: a navigator in monoclonal antibody development and applications". *The oncologist* 12.12 (2007), pp. 1379–1389.

[5] N. B. Sobol, J. A. Korsen, A. Younes, et al. "ImmunoPET Imaging of Pancreatic Tumors with 89 Zr-Labeled Gold Nanoparticle–Antibody Conjugates". *Molecular imaging and biology* 23 (2021), pp. 84–94.

[6] D. P. Cormode, E. Roessl, A. Thran, et al. "Atherosclerotic plaque composition: analysis with multicolor CT and targeted gold nanoparticles". *Radiology* 256.3 (2010), pp. 774–782.

[7] R. Meir, K. Shamalov, O. Betzer, et al. "Nanomedicine for cancer immunotherapy: tracking cancer-specific T-cells in vivo with gold nanoparticles and CT imaging". *ACS nano* 9.6 (2015), pp. 6363–6372.

[8] C. T. Badea, M Holbrook, D. P. Clark, et al. "Spectral imaging of iodine and gadolinium nanoparticles using dual-energy CT". *Medical Imaging 2018: Physics of Medical Imaging*. Vol. 10573. SPIE. 2018, pp. 375–381.

[9] C. T. Badea, D. P. Clark, M Holbrook, et al. "Functional imaging of tumor vasculature using iodine and gadolinium-based nanoparticle contrast agents: a comparison of spectral micro-CT using energy integrating and photon counting detectors". *Physics in Medicine & Biology* 64.6 (2019), p. 065007.

[10] W. P. Segars, B. M. Tsui, E. C. Frey, et al. "Development of a 4-D digital mouse phantom for molecular imaging research". *Molecular Imaging & Biology* 6.3 (2004), pp. 149–159.

[11] C. Syben, M. Michen, B. Stimpel, et al. "PYRO-NN: Python reconstruction operators in neural networks". *Medical physics* 46.11 (2019), pp. 5110–5115.

[12] A. M. Hernandez and J. M. Boone. "Tungsten anode spectral model using interpolating cubic splines: unfiltered x-ray spectra from 20 kV to 640 kV". *Medical physics* 41.4 (2014), p. 042101.

[13] J. Punnoose, J Xu, A. Sisniega, et al. "spektr 3.0—A computational tool for x-ray spectrum modeling and analysis". *Medical physics* 43.8Part1 (2016), pp. 4711–4717.